Original Paper

Eletrônica de Potência
Open Journal of Power Electronics

Received August 05, 2024; accepted December 12, 2024; Date of publication January 20, 2025.
The review of this paper was arranged by Associate Editor Montiê A. Vitorino and Editor-in-Chief Heverton A. Pereira.

Digital Object Identifier http://doi.org/10.18618/REP.e202508

Four-level Resonant Flying Capacitor Converter Operating under Resonance Featuring Soft-Switching and Voltage Regulation Capabilities

Augusto M. Medeiros[1,2], **Yales R. de Novaes**[1]

[1]State University of Santa Catarina, NPEE, Department of Electrical Engineering, Joinville, SC, Brazil.
[2]OAK Amplifiers AB, Kungsbacka, Sweden.

e-mail: augustomanfroimedeiros@gmail.com; yales.novaes@udesc.br.

ABSTRACT Multilevel resonant converter topologies have been addressed to increase the power density and efficiency of step-down intermediate conversion stages, for low-voltage (LV) systems, due to the higher current demand, in addition to its inherent benefit of soft-switching capability and fixed static-gain ratio, while operating at, or above, resonance. This work proposes an extension for the multilevel Resonant Flying Capacitor Converter (ML-RFLCC), by demonstrating the potential soft-switching and voltage regulation capabilities of a 1:3 RFLCC while operating under and at the resonance. Due to the increased number of state variables, it presents a comprehensive state diagram, and normalization framework, to demonstrate the operating principle, and dependencies, of the different set of LC resonant tanks. In order to achieve such an operation, this work proposes an operating condition coefficient Λ to derive a design methodology. To validate the proposed operation condition, a 400V 500W GaN-based 1:3 RFLCC is presented, illustrating the theoretical correlation and non-idealities while operating under resonance.

KEYWORDS DC/DC Conversion, Flying-Capacitor, Multi-Resonant, State-plane Trajectory, WBG Devices.

I. INTRODUCTION

DC-DC step-up and step-down power converters have been extensively utilized over the years in a broad range of applications from DC distribution networks [1], to renewable energy systems, to lower voltage applications such as datacenters and telecommunications [2] and low-voltage digital circuitry [3] [4], where the conversion ratio and output current requirements are usually high. As a consequence, high efficiency and high power density converters become important in order to achieve a high level of sustainability.

To fulfill such requirements, either multi-stage conversion architectures have been widely employed, in order to overcome the poor performance of conventional buck-like or boost-like converters operating with a large conversion ratio, or, alternatively, isolated DC-DC converters, due to their ability of increasing the conversion ratio based on a magnetically coupling component to support the large conversion ratio [1] [5]. Even though multi-stage conversion architectures can potentially achieve good levels of power density and compactness [5], the additional stages generally require bulky energy storage elements either to decouple the conversion stages, or to enable a better utilization of two-level (2L) buck-like or boost-like converter.

Due to these distinct conditions, multi-level converters have been addressed in order to optimize the system's performance due to its ability to deliver a higher conversion ratio, lower volt-second balance in inductors, in case of magnetic-type converter, as well as the feasibility to utilize lower voltage switches [6] which leads to better Figure-of-Merits (FoM) compared to high voltage switches. Amongst the different structures that are defined as multi-level converters, switched-capacitor-like converters have been widely utilized due to their key benefits such as the magnetic-less characteristic but lack of flexibility to fulfill a particular voltage gain requirement, except fixed integers voltage gains, in comparison to their natural counter-parts such as conventional buck or boost converters. Such characteristics generally lead to higher power density and small component count. On the other hand, due to the magnetic-less characteristic, large current spikes are experienced due to the charging/discharging process of the intermediate capacitors [7] and, consequently, lower efficiency is achievable. Therefore, such topology becomes limited to lower output current and/or lower input voltage applications.

In order to tackle this limitation, hybrid structures have been explored, introducing an inductor to limit the capacitive charge loss which, inevitably, leads to a reduction in the power density due to the increased total passive component volume. An alternative solution, which harmonizes with the inductor's introduction, is the FLCC (Flying Capacitor Converter). It introduces similar behavior with an inherent possibility of exploring the intertwined nature of the passive

components in different ways, as presented in Fig. 1, depending on C_{FLY}'s state of charge and the active switches $S_1 - S_2$'s state.

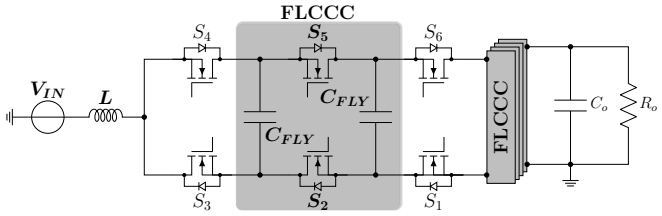

FIGURE 1. Schematic Representation of a Generic N-Level Flying Capacitor Converter (ML-FLCC) with N-1 Flying Capacitor Commutation Cells (FLCCC)

Despite of the benefits of the above-mentioned topology, and number of levels, it holds limitations in terms of efficiency, power density and EMC performance as it often operates under hard-switching condition and the total passive component volume is high. RFLCC (Resonant Flying Capacitor Converter) addresses these limitations as it enables the operation at higher switching frequency while having lower switching losses and electromagnetic emissions (EME). Cascaded topologies have also been explored in resonant mode, where cascaded stages are decoupled by a bulky element [2], and also where the intermediate passive components are simplified to optimize the passive component count and total volume, as demonstrated by [8], and [9] which integrates a switched-capacitor, to form a switching virtual bus, interweaving its operating with adjacent RFLCC modules, leading to reduction in complexity and resonant tank's total volume.

The ability of the above-mentioned converters to greatly increase the power density is also driven by the passive components volume given the objective of defining the characteristic impedance to balance, and optimize, the energy utilization of the resonant tank components, such as the resonant inductor and resonant capacitor [10] [11], where [10] addresses this issue by defining the energy utilization and comparing the characteristic impedance of different switched capacitors. On the contrary, [12] [13] defines a conduction mode factor as the variable for efficiency optimization objective whereas [14] [9] introduce ZVS cross-conduction time to secure ZVS condition while operating the RFLCC above resonance.

The majority of the past, and recent, work have explored the flying capacitor resonant converter as a non-regulated step-up or step-down converter with a given characteristic of fixed conversion ratio while operating above, or at, resonance due to the possibility of achieving ZVS and reduced current stresses.

This present work expands the utilization of RFLCC to address higher-voltage applications (up to 400V) and the RFLCC operation under resonance contributing with a comprehensive description of the different equivalent circuits and the ability of the proposed converter to fulfill variable voltage conversion ratio G and maintaining soft-switching condition while operating under the right operating condition. The rest of the article is organized as follows: Section II describes the proposed 4L-RFLCC, shown in Fig. 2, emphasizing the possible different LC resonant tank configurations, where key equations determining the analytical and geometrical representation are revisited, and the resultant static-gain and large-signal properties, where the major properties of duality is shown, emphasizing the possibility of ZCS and ZVS. Next, Section V discloses the design methodology and validates the analysis of Section II using a GaN-based converter. Finally, Section VI summarizes the findings in the article and provides the final considerations.

II. PROPOSED CONVERTER

Fig. 2 shows the 4L-RFLCC under evaluation. It consists of three low-side switches and three high-side switches, denoted as $S_1 - S_3$ and $D_4 - D_6$, respectively, and one resonant inductor L_r and two resonant capacitors C_{r_1} and C_{r_2}, which exhibits the same capacitance C_r. This architecture is capable of achieving a 1:3 conversion ratio when the switching transitions are phase-shifted by 120° and the pulse-width is equivalent approximately 0.667% $\left(D = \frac{2}{3}\right)$. As a result of the proposed PWM strategy, two active switches are always simultaneously ON, as shown in Table 1, whereas the passive switches' states depend on the converter's operating condition.

TABLE 1. List of Active Switches Transition Events.

Transition Event	Switches State		
	S_1	S_2	S_3
⑪	ON↑	ON	OFF↓
㉑	ON	OFF ↓	ON ↑
㉛	OFF ↓	ON ↑	ON

Therefore, three possible resonant tanks are present in the proposed operation. In a generic form, the resonant activity is composed by the series connection of at least one L_r and one C_r upon the excitation of either a single-ended or a differential-mode voltage, with known state variables' initial condition $v_{C_{r_n}}(0)$ and $i_{C_{r_n}}(0)$, and are further described in the next Section.

A. A $N_P : N_S$ GENERIC RESONANT TANK DESCRIPTION

The series resonance description has been described in details in [15] while this section expands the description with the generalized form considering the series and parallel connections of C_r. Fig. 3 exhibits the three different resonant tank configurations, in which $m \times S_n$ denotes the number of ***m*** devices in series within the ***n-th*** current path, where

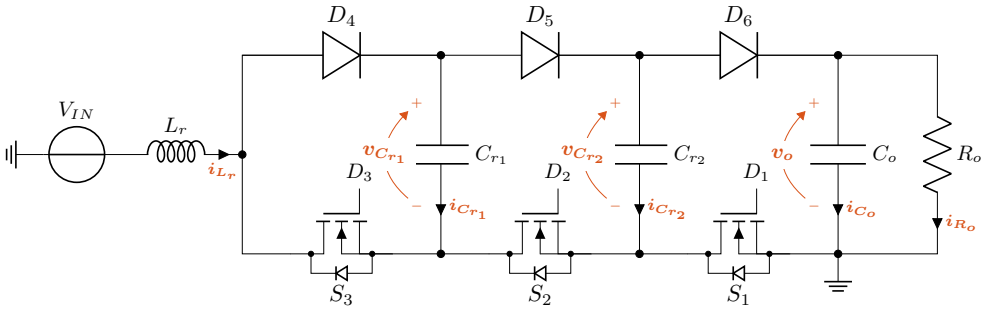

FIGURE 2. Schematic for the Proposed 4L-RFLCC. The state variables are highlighted in red

and are mainly related to the resonant capacitors' current $i_{C_{r_n}}$ and voltage's $v_{C_{r_n}}$ where $n \in \{1, 2\}$.

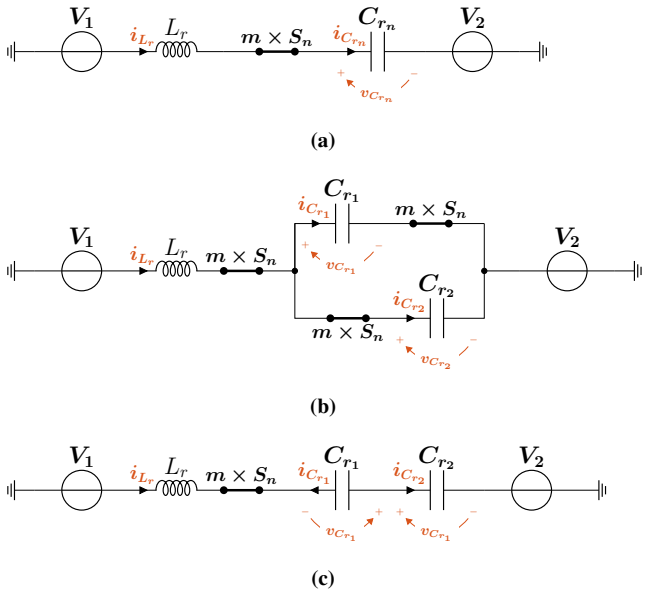

FIGURE 3. Feasible LC Equivalent Resonant Tank Configuration for the Proposed 4L-RFLCC:
((a)) Type I - $L_r C_r$ **Resonant Tank**
((b)) Type II - $L_r\left(C_{r_1} \parallel C_{r_2}\right)$ **Resonant Tank**
((c)) Type III - $L_r C_{r_1} C_{r_2}$ **Resonant Tank**

V_1 and V_2 represent two arbitrary voltage-sources applied differentially across the resultant resonant tank.

Letting (1) be the generalized description of the equivalent resonant tank configurations.

$$-V_1 + v_{L_r}(t) + \sum_{n=0}^{N_s} \left(\pm v_{C_{r_n}}(t)\right) + V_2 = 0 \tag{1}$$

Thus, the resultant set of resonant characteristics are derived given the number of series N_s and parallel N_p connections of resonant capacitors C_r, resulting in the following:

$$i_{L_r}(t) = \sum_{m=0}^{N_p} \left(\pm i_{C_{r_n}}(t)\right) \tag{2}$$

where $i_{L_r}(t)$ and $i_{C_r}(t)$ are by definition correlated with:

$$v_{L_r}(t) = L_r \cdot \frac{di_{L_r}(t)}{dt} \tag{3}$$

$$i_{C_r}(t) = C_r \cdot \frac{dv_{C_r}(t)}{dt} \tag{4}$$

In order to have a comprehensive assessment, $\boldsymbol{N_s}$ and $\boldsymbol{N_p}$ are analyzed independently. Thus, by assuming $\boldsymbol{N_p}$, and substituting (2) and (3) into (1), the resultant state variables are found.

$$v_{C_r}(t) = \pm V_{DM} - \left(\pm V_{DM} - V_{C0}\right) \cdot \cos(\omega_n t) \pm \ldots \\ \cdots \pm Z_{r_n} I_{L0} \cdot \sin(\omega_n t) \tag{5}$$

$$i_{L_r}(t) = \left(\frac{\pm V_{DM} - V_{C0}}{Z_{r_m}}\right) \cdot \sin(\omega_m t) + \ldots \\ \cdots + I_{L0} \cdot \cos(\omega_m t) \tag{6}$$

where Z_{r_m} and ω_m are the resultant characteristic impedance and resonant frequency, respectively, and V_{DM} corresponds to the differential voltage applied across the equivalent resonant tank, defined as follows:

$$Z_{r_m} = \frac{1}{\sqrt{N_p}} \cdot \sqrt{\frac{L_r}{C_r}} = \frac{1}{\sqrt{N_p}} \cdot Z_r \tag{7}$$

where Z_r is the global reference characteristic impedance, and defined as followed:

$$Z_r = \sqrt{\frac{L_r}{C_r}} \tag{8}$$

$$\omega_m = \frac{1}{\sqrt{N_p}} \cdot \frac{1}{\sqrt{L_r C_r}} = \frac{1}{\sqrt{N_p}} \cdot \omega_0 \tag{9}$$

$$V_{DM} = V_1 - V_2 \tag{10}$$

Finally, by applying (6) into (4), the expression for $i_{C_{r_m}}$ is derived.

$$i_{C_{r_m}}(t) = \frac{1}{N_p} \cdot \left(\frac{\pm V_{DM} - V_{C0}}{Z_{r_m}}\right) \cdot \sin(\omega_m t) + \ldots \\ \cdots + \frac{1}{N_p} \cdot I_{L0} \cdot \cos(\omega_m t) \tag{11}$$

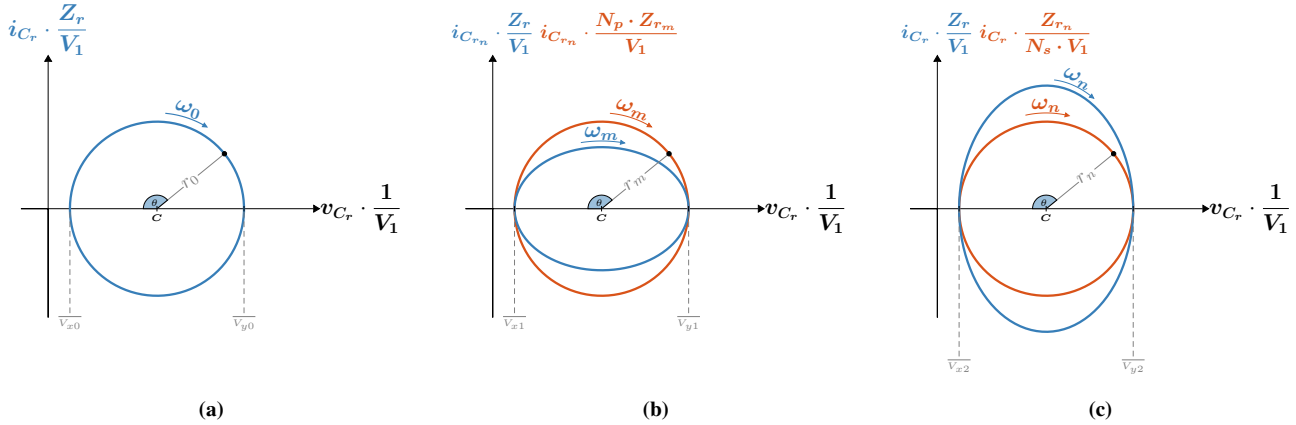

FIGURE 4. Resultant State-Plane Trajectory for: (a) Type I - L_rC_r Resonant Tank; (b) Type II - $L_r\left(C_{r_1} \parallel C_{r_2}\right)$ Resonant Tank and (c) Type III - $L_rC_{r_1}C_{r_2}$ Resonant Tank; where the solid-blue trajectory corresponds to the Z_r reference frame, also defined as the global reference frame, whereas the solid-red trajectory corresponds to the equivalent Z_{r_j} reference frame, also defined as local reference frame, where $j \in \{m, n\}$.

Similarly, by solving for $\boldsymbol{N_s}$, the following state variables are found.

$$i_{L_r}(t) = \left(\frac{V_{DM} - \sum_{n=0}^{N_s} \left(\pm V_{C_{r_n}}(0) \right)}{Z_{r_n}} \right) \cdot \sin(\omega_n t) + \ldots$$
$$\ldots + I_{L0} \cdot \cos(\omega_n t) \tag{12}$$

$$i_{C_r}(t) = \pm \left(\frac{V_{DM} - \sum_{n=0}^{N_s} \left(\pm V_{C_{r_n}}(0) \right)}{Z_{r_n}} \right) \cdot \sin(\omega_n t) \pm \ldots$$
$$\ldots \pm I_{L0} \cdot \cos(\omega_n t) \tag{13}$$

Therefore, substituting (13) into (4), the expression for $v_{C_{r_n}}$ is derived.

$$v_{C_{r_n}}(t) = V_{C_{r_n}}(0) \pm \frac{1}{N_s} \cdot \left(V_{DM} - \sum_{n=0}^{N_s} \left(\pm V_{C_{r_n}}(0) \right) \right) \cdot$$
$$\cdot \left(1 - \cos(\omega_n t)\right) \pm \frac{1}{N_s} \cdot Z_{r_n} \cdot I_{L0} \cdot \sin(\omega_n t) \tag{14}$$

where Z_{r_n} and ω_n are the resultant characteristic impedance and resonant frequency, respectively, defined as follows:

$$Z_{r_n} = \sqrt{N_s} \cdot \sqrt{\frac{L_r}{C_r}} = \sqrt{N_s} \cdot Z_r \tag{15}$$

$$\omega_n = \sqrt{N_s} \cdot \frac{1}{\sqrt{L_r C_r}} = \sqrt{N_s} \cdot \omega_0 \tag{16}$$

Comparing both cases, although their characteristics are predominantly sinusoidal, they differ with respect to the resultant voltage and current due to N_p and N_s. Analytically, the above-mentioned expressions are not very intuitive. Thus, given the sinusoidal waveform, a geometrical representation is derived to better visualize the impact of N_p and N_s. By manipulating (5) and (11), the type II can be interpreted in different ways, depending on the defined reference framework. Given the resonant characteristics, presented in (9) and (7), two different reference frameworks are derived to represent the system geometrically, as shown in (17) and (18).

$$\overline{i(t)} = i(t) \cdot \frac{Z_r}{V_1} \tag{17}$$

$$\overline{\overline{i(t)}} = i(t) \cdot \sqrt{N_p} \cdot \frac{Z_r}{V_1} = \sqrt{N_p} \cdot \overline{i(t)} \tag{18}$$

Thus, the two different type II's geometrical representations are derived, as shown in (19) and (20), exhibiting two different geometrical meanings.

$$\left(\overline{v_{C_r}(t)} - \overline{V_{DM}} \right)^2 + \left(\overline{\overline{i_{C_{rm}}(t)}} \right)^2 =$$
$$\left(\pm \overline{V_{DM}} - \overline{V_{C0}} \right)^2 + \left(\frac{1}{N_p} \right)^2 \cdot \overline{\overline{I_{L0}}}^2 \tag{19}$$

$$\left(\overline{v_{C_r}(t)} - \overline{V_{DM}} \right)^2 + \frac{\left(\overline{i_{C_{rm}}(t)} \right)^2}{\left(\frac{1}{N_p} \right)^2} =$$
$$\left(\pm \overline{V_{DM}} - \overline{V_{C0}} \right)^2 + \left(\frac{1}{\sqrt{N_p}} \cdot \overline{I_{L0}} \right)^2 \tag{20}$$

Equation (19) corresponds to a circular geometry, whereas (20) causes a stretch in the $i(t)$ state variable; therefore, leading to an elliptical geometry, as shown in Fig. 4(b).

Similarly, the type III is represented under two different reference frameworks, where the first one is shared with the type II, as shown in (17), whereas the second reference framework is unique to the type III resonant tank configuration, derived in (24).

$$\overline{\overline{i\left(t\right)}} = i\left(t\right) \cdot \frac{1}{\sqrt{N_s}} \cdot \frac{Z_r}{V_1} = \frac{1}{\sqrt{N_s}} \cdot \overline{i\left(t\right)} \tag{21}$$

Thus, by manipulating (13) and (14), the two different type III's geometrical representations are derived, as shown in (22) and (23).

$$\begin{aligned} &\left(\begin{array}{l} \overline{v_{C_{r_n}}\left(t\right)} - \overline{V_{C_{r_n}}}\left(0\right) + \cdots \\ \cdots \mp \dfrac{1}{N_s} \cdot \left(\overline{V_{DM}} - \displaystyle\sum_{n=0}^{N_s} \left(\pm \overline{V_{C_{r_n}}}\left(0\right) \right) \right) \end{array} \right)^2 + \\ &+ \left(\overline{\overline{i_{C_r}\left(t\right)}} \right)^2 = \\ &= \overline{\overline{I_{L0}}}^2 + \left(\frac{1}{N_s} \right)^2 \cdot \left(\overline{V_{DM}} - \sum_{n=0}^{N_s} \left(\pm \overline{V_{C_{r_n}}}\left(0\right) \right) \right)^2 \end{aligned} \tag{22}$$

$$\begin{aligned} &\left(\begin{array}{l} \overline{v_{C_{r_n}}\left(t\right)} - \overline{V_{C_{r_n}}}\left(0\right) + \cdots \\ \cdots \mp \dfrac{1}{N_s} \cdot \left(\overline{V_{DM}} - \displaystyle\sum_{n=0}^{N_s} \left(\pm \overline{V_{C_{r_n}}}\left(0\right) \right) \right) \end{array} \right)^2 + \\ &+ \frac{\left(\overline{i_{C_r}\left(t\right)} \right)^2}{\left(\sqrt{N_s} \right)^2} = \\ &= \frac{\overline{I_{L0}}^2}{\left(\sqrt{N_s} \right)^2} + \left(\frac{1}{N_s} \right)^2 \cdot \left(\overline{V_{DM}} - \sum_{n=0}^{N_s} \left(\pm \overline{V_{C_{r_n}}}\left(0\right) \right) \right)^2 \end{aligned} \tag{23}$$

Equation (22) corresponds to a circular geometry, whereas (23) causes a stretch in the $i\left(t\right)$ state variable; therefore, leading to an elliptical geometry, as shown in Fig. 4(c).

$$\overline{\overline{i\left(t\right)}} = i\left(t\right) \cdot \frac{1}{\sqrt{N_s}} \cdot \frac{Z_r}{V_1} = \frac{1}{\sqrt{N_s}} \cdot \overline{i\left(t\right)} \tag{24}$$

B. OPERATING PRINCIPLES

Given the switches state, shown in Table 1, and the passive characteristics of switches $D_4 - D_6$, the operating principle depends on C_{r_n}'s state of charge $V_{C_{r_n}}\left(0\right)$, where 0 refers to the initial condition upon the transition event's trigger. Given the C_{r_n}'s initial voltage condition $V_{C_{r_n}}\left(0\right)$, where $n \in \{1, 2\}$, described as G_{1III} and G_{2III}, the (11) exhibits two different possible operating principles. At (11), the switches S_1 and S_3 turn-ON and OFF, respectively, while S_2 remains in ON-state, resulting in a conditional charging state, when diode D_4 forward biases.

Due to V_{IN} excitation upon the type I $L_r C_{r_1}$'s resonant tank, and $V_{C_{r_1}}\left(0\right) = G_{1III}$, (25) governs the C_{r_1}'s state plane trajectory, also shown in Fig. 5(a).

$$\left(\overline{v_{C_{r_1}}}\left(t\right) - 1 \right)^2 + \left(\overline{\overline{i_{C_{r_1}}}}\left(t\right) \right)^2 = \left(1 - G_{1III}\right)^2 \tag{25}$$

By interpreting (25), the first charging phase yields the following possible conditions:

$$\overline{I_{C_{r_1}\langle pk \rangle}} = \frac{\Delta \overline{V_{C_{r_1}}}}{2} = 1 - G_{1III} \tag{26}$$

where C_{r_1}'s maximum current and voltage swing depend on its initial voltage condition.

Because of $S_1 - S_3$'s switches state, within the first charging phase, C_{r_2}'s state of charge is relevant given the possibility to trigger a forward-bias mechanism in the diode D_5, leading to the second charging phase, by fulfilling the following condition.

$$G_{2III} < 2 - G_{1III} \tag{27}$$

In case (27) is not met, diode D_5 remains blocked and the first charging state lasts for a full resonant cycle. On the other hand, in case (27) is met, the charging phase undergoes a split-charge mechanism where the diode D_5 forward biases, leading to a type II $L_r\left(C_{r_1} || C_{r_2}\right)$'s resonant tank configuration. This phenomenon is highlighted by a instantaneous change of the natural impedance imposed by the resonant tank; thus, yielding a change in the ongoing resonant activity. Due to the C_{r_n}'s parallel connection, the following characteristics, as per (19) and (20), govern the operating principle within the remaining of the charging phase.

$$\begin{aligned} &\left(\overline{v_{C_r}\left(t\right)} - 1 \right)^2 + \frac{\left(\overline{i_{C_r}\left(t\right)} \right)^2}{\left(\frac{1}{2} \right)^2} = \\ &\left(1 - G_{2III}\right)^2 + \left(\frac{1}{2} \cdot \frac{\omega_1}{\omega_0} \cdot \overline{I_{2III}} \right)^2 \end{aligned} \tag{28}$$

$$\begin{aligned} &\overline{I_{C_{r_n}\langle pk \rangle}} = \frac{\omega_0}{\omega_1} \cdot \left(G_{3III} - 1\right) = \\ &\frac{\omega_0}{\omega_1} \cdot \sqrt{ \begin{array}{l} \left(1 - G_{2III}\right)^2 + \cdots \\ \cdots + \left(\dfrac{1}{2} \cdot \dfrac{\omega_1}{\omega_0} \cdot \overline{I_{2III}} \right)^2 \end{array} } \end{aligned} \tag{29}$$

where I_{2III} is the C_{r_1}'s current condition when the first charging phase seizes.

$$\omega_0 \cdot \Delta T_{1III} = \arccos\left(\frac{1 - G_{2III}}{1 - G_{1III}} \right) \tag{30}$$

$$\omega_1 \cdot \Delta T_{2III} = \frac{\pi}{2} - \arctan\left(\frac{\sqrt{2} \cdot \left(1 - G_{2III}\right)}{\overline{I_{2III}}} \right) \tag{31}$$

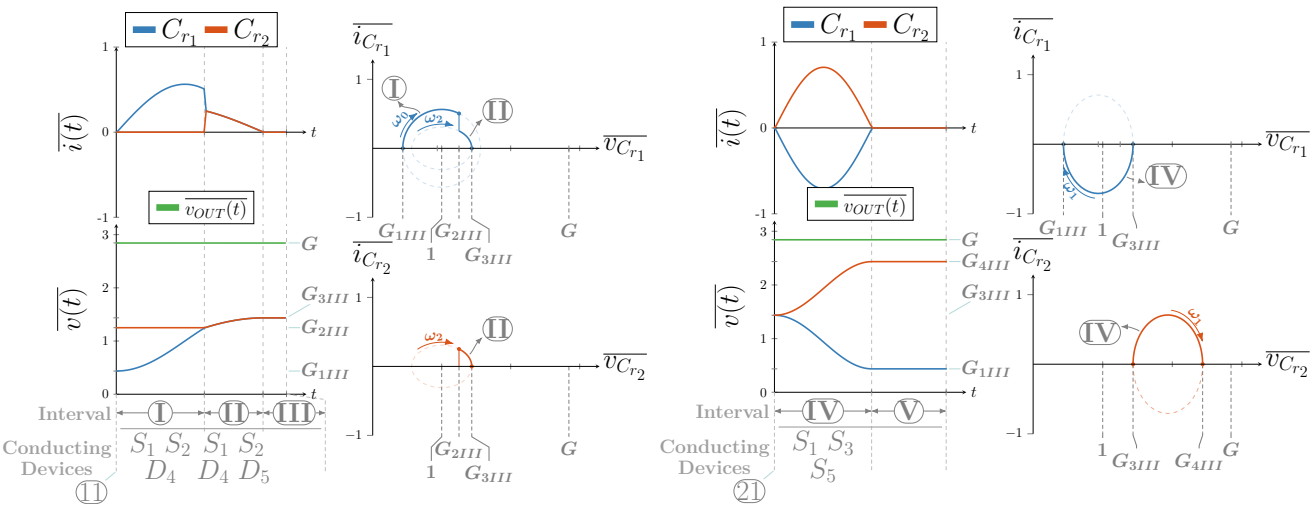

FIGURE 5. Normalized Time-domain and State-plane trajectory upon: (a) Transition Event (11); (b) Transition Event (21); highlighting the different possible states and operating principles, depending on $V_{C_{r_n}}(0)$, when operating the proposed converter under variable voltage gain condition.

Due to the under resonance operation, the charging cycle is completed and the converter remains in Idle State.

The transition event (21) is highlighted by C_{r_1}'s charge being transferred to the upstream capacitors given the switches $S_2 - S_3$ turning OFF and ON, respectively, while Switch S_1 remains in ON-state. Due to C_{r_n}'s initial voltage conditions, diode D_5 forward biases, leading to a change of polarity in C_{r_1} and transferring its charge to C_{r_2}. Due to the V_{IN} excitation upon the type III's $L_r C_{r_1} C_{r_2}$'s resonant tank, and $\overline{V_{C_r}}(0) = G_{3III}$, (32) describes the C_{r_n}'s state plane trajectory, as shown in Fig. 5(b).

$$\left(\overline{v_{C_{r_n}}}(t) - G_{3III} \mp \frac{1}{2}\right)^2 + \frac{\left(\overline{i_{C_r}}(t)\right)^2}{\left(\sqrt{2}\right)^2} = \left(\frac{1}{2}\right)^2 \quad (32)$$

where sign and sign correspond to the C_{r_2} and C_{r_1} charging and discharging sign, respectively. By interpreting (32), it yields the following conditions:

$$\left|\overline{I_{C_{r_n}\langle pk\rangle}}\right| = \frac{\Delta \overline{V_{C_{r_n}}}}{2} = \frac{1}{2} \cdot \frac{\omega_2}{\omega_0} = \sqrt{2} \quad (33)$$

By assuming that the output voltage G is always one unit away from G_{3III}, the charge-transfer state lasts for a full resonant cycle, initiating and concluding under zero-current condition. Due to the equivalent ω_2, the converter undergoes a second idle state, based on (34).

$$\frac{\Delta T_{4III}}{\omega_2} + \Delta T_{5III} = \frac{1}{3} \cdot \frac{1}{f_{SW}} \quad (34)$$

Lastly, upon the transition event (31), when switches $S_1 - S_2$ turns OFF and ON, respectively, while switch S_3 remains

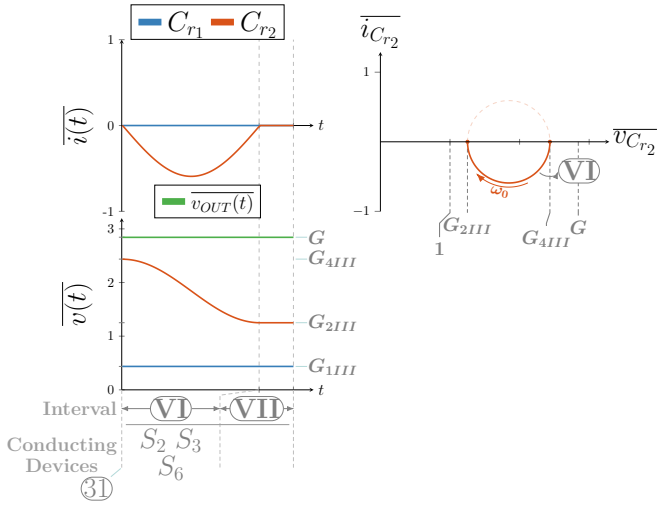

FIGURE 6. Normalized Time-domain and State-plane Trajectory upon the Transition State (31) highlighting the two possible charging states depending on $V_{C_{r_n}}(0)$

in ON-state, the C_{r_2}'s accumulated charge is discharged to the output given diode D_6's forward biasing mechanism due to G and C_{r_2}'s initial G_{4III}'s condition. Upon the $V_{IN} - V_{OUT}$ excitation across the type I's $L_r C_{r_2}$'s resonant tank, (35) describes the C_{r_2}'s state plane trajectory, as shown in Fig. 6.

$$\left(\overline{v_{C_{r_2}}}(t) - (G-1)\right)^2 + \left(\overline{\overline{i_{C_{r_2}}}}(t)\right)^2 = \left(G_{4III} - (G-1)\right)^2 \quad (35)$$

By interpreting (36), the discharging phase yields the following conditions:

$$\overline{I_{C_{r_2}\langle pk\rangle}} = \frac{\Delta\overline{V_{C_{r_2}}}}{2} = G_{4III} - G + 1 \tag{36}$$

Although there exist many unknown variables, the state-plane trajectories reveal an important property about a DC voltage level in which each of the resonant Capacitor's voltage swing in between. Upon the transition event (31), although the trajectory's center depends on G, the symmetrical behavior demonstrate this property as shown in (35) and (36), for the resonant capacitor C_{r_2}. Differently, due to the split-charge mechanism, a DC voltage level based on a standalone interval is not valid. Therefore, by interpreting (25) and (28), it reveals that within the same charging state, regardless of exhibiting a split-charge phase, the resonant capacitor C_{r_1} retains the DC voltage level in which $v_{C_{r_1}}(t)$ fluctuates in between.

$$\overline{v_{C_{r_1}}}(t) = 1 \pm \Delta\overline{v_{C_{r_1}}} \tag{37}$$

$$\overline{v_{C_{r_2}}}(t) = G - 1 \pm \Delta\overline{v_{C_{r_2}}} \tag{38}$$

Since C_{r_2} carries the output load current I_{OUT}, (39) creates an interconnection between the total voltage swing, shown in (36) and the operating condition.

$$\int_{t_5}^{t_6} d\overline{v_{C_{r_2}}}(t)\ dt = \frac{1}{C_{r_2}} \cdot \int_{t_5}^{t_6} d\overline{i_{C_{r_2}}}(t)\ dt \tag{39}$$

By manipulating (39), it yields:

$$\Delta\overline{V_{C_{r_2}}} = \overline{I_{OUT}} \cdot \frac{2\pi}{\mu_0} \tag{40}$$

where μ_0 is the effective frequency ratio, defined in (41).

$$\mu_0 = \frac{2\pi \cdot f_{SW}}{\omega_0} \tag{41}$$

where r_o is the normalized output load impedance, defined in (42).

$$r_o = \frac{R_{OUT}}{Z_r} \tag{42}$$

Equation (39) indicates the dependency of both switching frequency and output load condition into the proportion of C_{r_2}'s voltage swing, leading to a dependency into G_{2III} and the phase-timing distribution within the split-charge intervals. Additionally, it yields the case assumption when the voltage swing is insufficient to culminate in a split-charge mechanism, resulting in a different and simplified operating principle. Consequently, altering the state-plane trajectories upon each transition event.

$$G_{2III} \propto \overline{I_{OUT}}, \mu_0 \tag{43}$$

$$\frac{\Delta T_{2III}}{\Delta T_{1III}} \propto \overline{I_{OUT}}, \mu_0 \tag{44}$$

Therefore, due to the insufficient voltage swing, the resonant capacitors' C_{r_1} and C_{r_2}'s maximum and minimum voltage become decoupled from each other, leading to the following statements:

$$MIN\left[\overline{v_{C_{r_2}}}(t)\right] \geq MAX\left[\overline{v_{C_{r_1}}}(t)\right] \tag{45}$$

$$\omega_0 \cdot \Delta T_{1IV} = cte = \pi \tag{46}$$

Fig. 7 represents the different resonant state variables and the state-plane trajectory, where the major difference is in the reduced current stress per phase as well as the asymptotes for both resonant capacitors given their full resonant cycle within its corresponding phase.

Fig. 9 and 10 exhibit the complete time-domain waveform and the state-plane trajectory for the state variables, respectively, as per the operating principles above-mentioned.

C. STATIC GAIN & LARGE-SIGNAL ANALYSIS

The static gain & large-signals, such as the peak currents, phase timings and intermediate voltage levels, are described based on a equilibrium state. As a result of the proposed operating principles, there exist three intrinsic resonant cycles, which are shown in Fig. 10, in which its characteristics are utilized to determine the unknown variables. In the case, where the 4L-RFLCC operates under resonance, and exhibits split-charge phases, the initial and final conditions, at the time instant t_i and t_f, respectively, are determined as $i_{L_r}(t_i) = i_{L_r}(t_f) = 0$. By utilizing the principle of capacitor's charge balance and inductor's volt-second balance, a system of equation is derived, resulting in a relationship amongst the intermediate voltage levels G_{1III}, G_{2III}, G_{3III} and G_{4III} and G.

$$\begin{cases} G_{1III} + 1 - G_{3III} = 0 \\ G_{3III} + 1 - G_{4III} = 0 \\ 1 - G_{2III} + G_{3III} - 2 \cdot (G_{4III} + 1 - G) = 0 \end{cases} \tag{47}$$

Similarly, the particular case, where the 4L-RFLCC no longer exhibits split-charge phases, the following system of equations is derived, resulting in a relationship amongst the intermediate voltage levels G_{1IV}, G_{2IV}, G_{3IV} and G_{4IV} and G.

$$\begin{cases} G_{2IV} - 2 + G_{1IV} = 0 \\ G_{1IV} + 1 - G_{3IV} = 0 \\ G_{4IV} - 1 - G_{2IV} = 0 \\ G_{3IV} + G_{4IV} - 2 \cdot (G - 1) = 0 \end{cases} \tag{48}$$

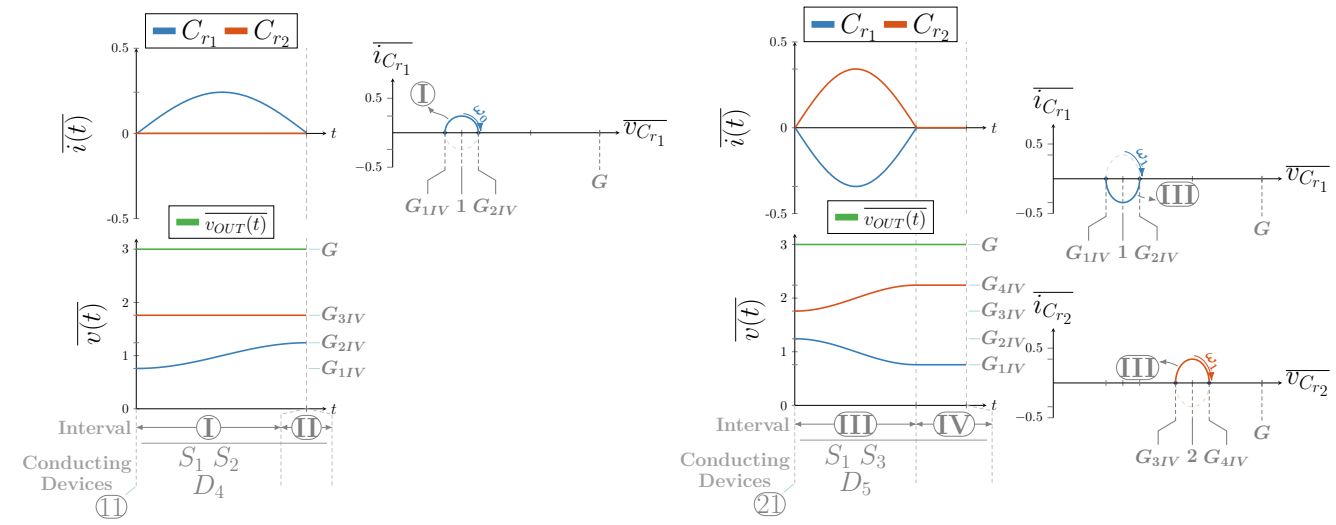

FIGURE 7. Normalized Time-domain and State-plane trajectory upon: (a) Transition Event (11); (b) Transition Event (21) under fixed voltage gain condition.

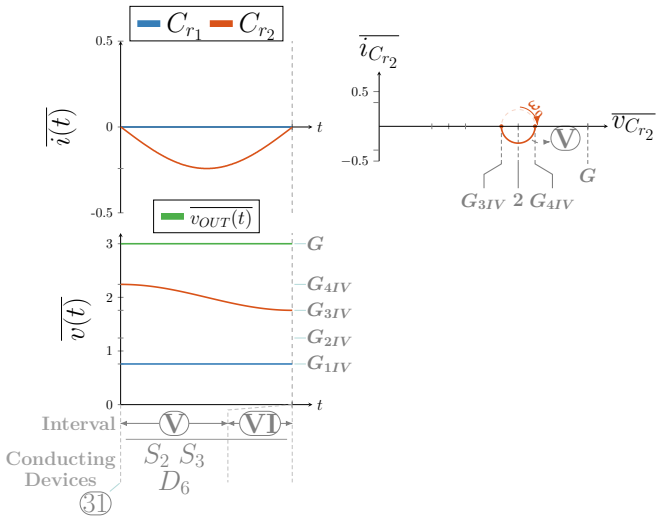

FIGURE 8. Normalized Time-domain and State-plane Trajectory upon the Transition State (31) under fixed voltage gain condition.

By manipulating (48), it yields the fixed voltage gain condition:

$$G = cte = 3 \tag{49}$$

On the other hand, due to the split-charge phases, Equation (47) derives three equations and five unknown variables. Therefore, two additional equations shall be derived in order to solve for the unknown variables within the variable voltage gain condition. The average input current $\overline{I_{IN}}$ and average output current $\overline{I_{OUT}}$ are derived.

$$\overline{I_{OUT}} = f_{sw} \cdot \int_{t_5}^{t_6} \overline{I_{S_6}(t)}\, dt \tag{50}$$

$$\begin{aligned}\overline{I_{IN}} &= f_{sw} \cdot \int_0^{T_{sw}} \overline{i_{L_r}(t)}\, dt = \\ &= \int_0^{\Delta T_{1III}} \overline{i_{L_{r10}}(t)}\, dt + 2 \cdot \int_0^{\Delta T_{2III}} \frac{1}{2} \cdot \overline{i_{L_{r21}}(t)}\, dt + \\ &+ \int_0^{\Delta T_{4III}} \overline{i_{L_{r43}}(t)}\, dt + \int_0^{\Delta T_{6III}} \overline{i_{L_{r65}}(t)}\, dt\end{aligned} \tag{51}$$

Solving (51), and (50), yield the final two required equations.

$$\overline{I_{OUT}} = \frac{\mu_o}{\pi} \cdot (G_{4III} + 1 - G) \tag{52}$$

$$\overline{I_{IN}} = \frac{\mu_o}{\pi} \cdot (9 + 3 \cdot G_{1III} - G_{2III} - 2 \cdot G) \tag{53}$$

By manipulating (53), and (52), and applying the energy conservation principle, the static-gain, as a function of the operating conditions, is derived.

$$G = 1 + \sqrt{1 + \frac{1}{2} \cdot \Lambda} \tag{54}$$

where Λ is defined as the operating condition coefficient.

$$\Lambda = \frac{r_o \cdot \mu_o}{\pi} \tag{55}$$

Substituting (54) into (47) yields the large-signal variables.

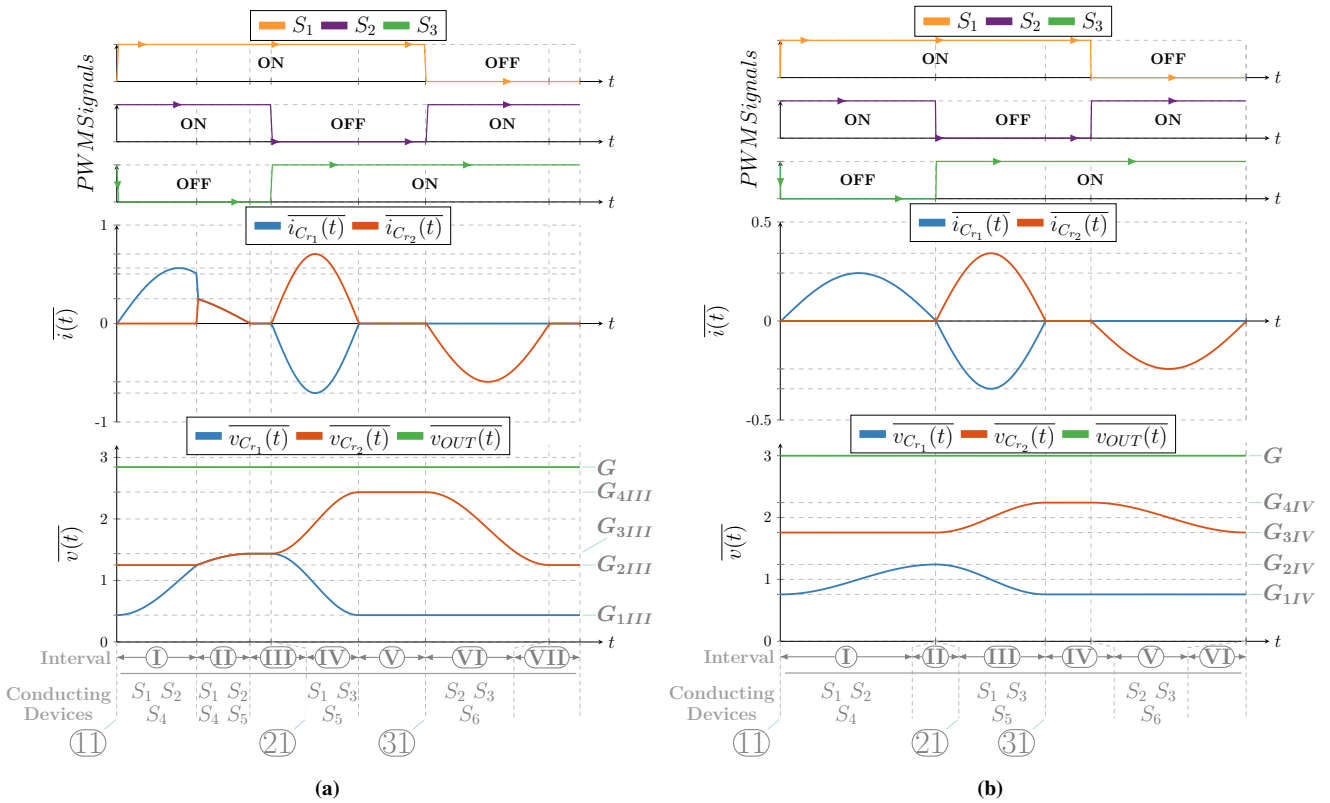

FIGURE 9. Normalized State Variables time-domain waveform representation under: (a) variable voltage gain condition and (b) fixed voltage gain condition.

$$G_{1III} = \frac{1}{\Lambda} - 2 + \left(1 + \frac{1}{\Lambda}\right) \cdot \sqrt{1 + \frac{1}{2} \cdot \Lambda} \tag{56}$$

$$G_{3III} = \frac{1}{\Lambda} - 1 + \left(1 + \frac{1}{\Lambda}\right) \cdot \sqrt{1 + \frac{1}{2} \cdot \Lambda} \tag{57}$$

$$G_{4III} = \frac{1}{\Lambda} + \left(1 + \frac{1}{\Lambda}\right) \cdot \sqrt{1 + \frac{1}{2} \cdot \Lambda} \tag{58}$$

$$G_{2III} = -\frac{1}{\Lambda} + \left(1 - \frac{1}{\Lambda}\right) \cdot \sqrt{1 + \frac{1}{2} \cdot \Lambda} \tag{59}$$

Based on (54) and the interpretation of the state-plane trajectories, the phase-timings can be derived, as shown in Fig. 11, demonstrating the split-charge mechanism according to the proposed converter's operating condition.

Note that the transition event ③① exhibits similar behavior under the two different cases. Therefore, (50) is utilized to solve for the large-signal variables as a function of the operating conditions, yielding the following.

$$G_{1IV} = 1 - \frac{3}{\Lambda} \tag{60}$$

$$G_{2IV} = 1 + \frac{3}{\Lambda} \tag{61}$$

$$G_{3IV} = 2 - \frac{3}{\Lambda} \tag{62}$$

$$G_{4IV} = 2 + \frac{3}{\Lambda} \tag{63}$$

As $\Delta\overline{v_{C_{r_n}}}(\Lambda)$ reduces, as function of Λ, so does the current stresses associated with each resonance cycle. Fig. 12 exhibits the peak current stresses within each resonant cycle as a function of the operating conditions. Additionally, Λ also reveals two different asymptotes, associated with C_{r_n}, derived from the state-plane trajectories, and the large-signal variables, as shown in (37) and (38).

$$\lim_{\Lambda \to \infty} \Delta\overline{v_{C_{r_n}}}(\Lambda) = 0 \tag{64}$$

where $n \in \{1, 2\}$ and $\Delta\overline{v_{C_{r_n}}}$ corresponds to the voltage swing across the resonant capacitors.

III. SOFT-SWITCHING CAPABILITY

Although operating the 4L-RFLCC under the resonance guarantees a zero-current switching (ZCS), it possesses a

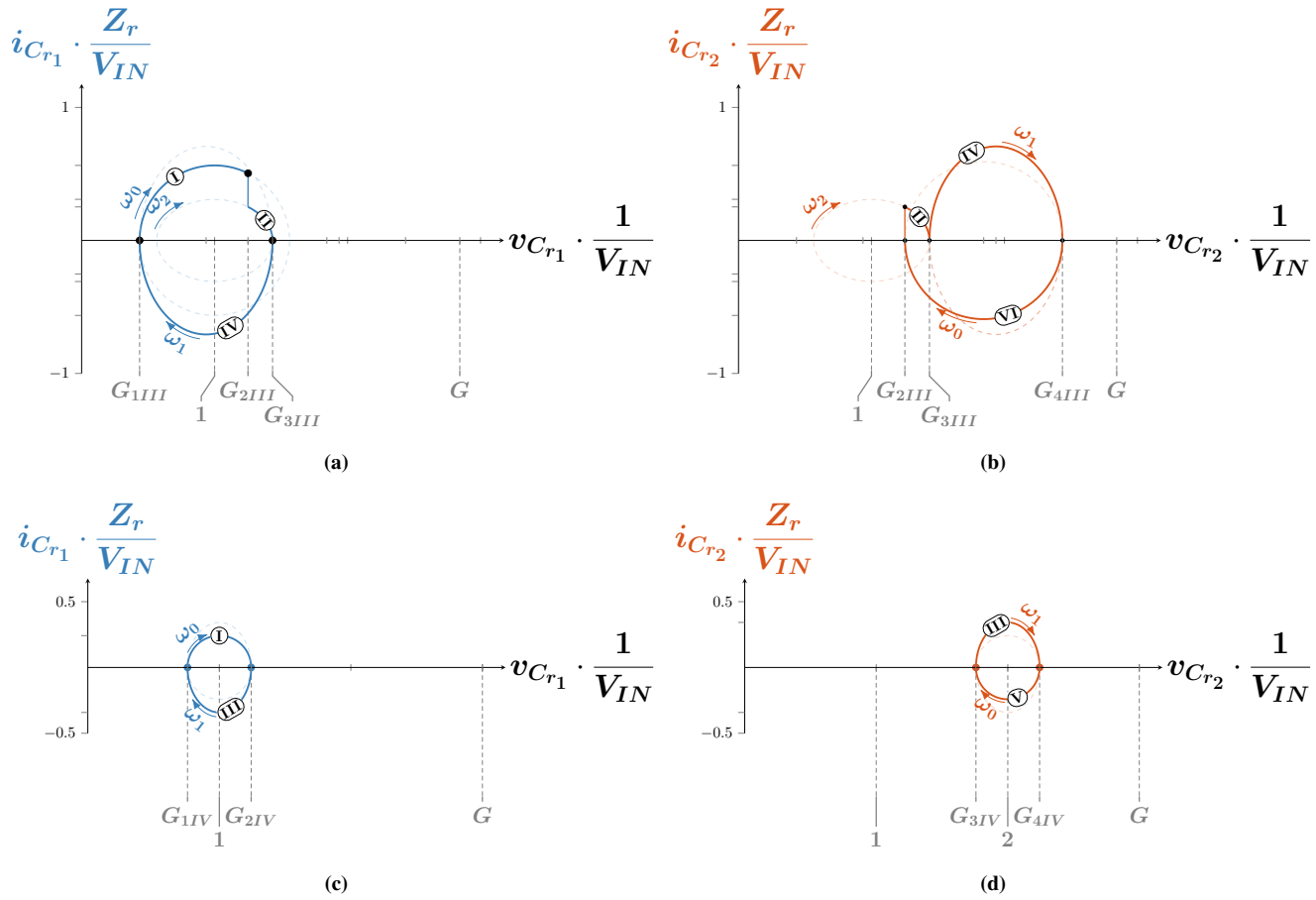

FIGURE 10. Normalized Complete State-plane trajectory for: (a) Resonant Capacitor C_{r_1} and (b) Resonant Capacitor C_{r_2} within the variable voltage gain condition and (c) Resonant Capacitor C_{r_1} and (d) Resonant Capacitor C_{r_2} within the fixed voltage gain condition.

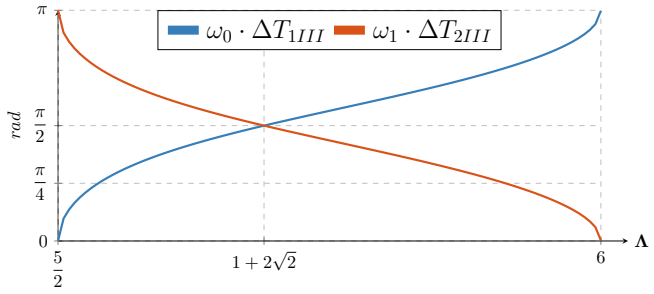

FIGURE 11. Split-phase timing under variable voltage gain condition as a function of Λ.

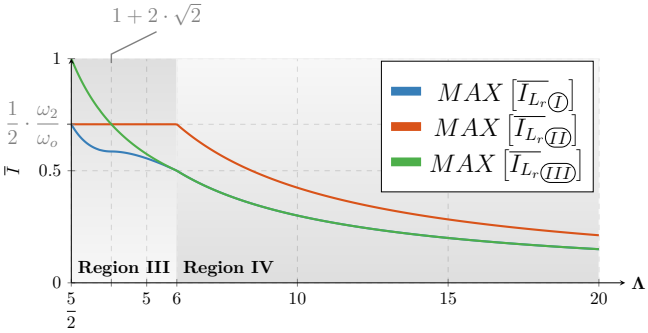

FIGURE 12. Phase-by-Phase Peak Current Stress exhibiting the effect of the operating condition into the potential conduction performance of the proposed 4L-RFLCC.

theoretical limitation to operate at very-high switching frequency range due to the inherent switches' C_{OSS}'s charge and discharge process. [12], [13] and [14] tackles the efficiency topic by exploring different operating frequencies and additional topological stages to secure higher efficiencies either by balancing the hard-switching losses, and the conduction losses, or by intentionally reversing the polarity of L_r's current to secure a zero-voltage switching (ZVS). [12] [13] explored the operation above resonance as a mean to reduce the conduction current stresses; thus, introducing hard-switching condition to every device. However, due to the lower input and output voltage ranges, and also the lower switching frequency, the impact of C_{OSS} and VI-overlap be-

come not as harmful to the overall efficiency. The conduction current stresses' reduction, by operating above the resonance, and intentionally not exhibiting a complete resonant cycle, has an equivalent effect, as shown in Section II, where the 4L-RFLCC retains the ability to reduce the current stresses while operating at high Λ conditions, demonstrated in Fig. 12. On the contrary, the hard-switching losses have a major impact on the overall efficiency for higher-voltage system.

Section II demonstrated the modulation strategy, alongside the transition events, where it highlights the diodes' $D_4 - D_5$ forward-biasing mechanism, which is fundamental for the assessment of the soft and hard-switching transitions, depending on the operating condition. Fig. 13 defines a FLCCC, demonstrated by the switch pair S_2D_5 and adjacent capacitors C_{r_1} and C_{r_2}. Similarly, there exist a second FLCCC, composed by the switch pair S_1D_6 and adjacent capacitors C_{r_2} and C_o.

The FLCCC culminates in a differential voltage across the switch pairs, defined by (65).

$$\begin{aligned} &\overline{v_{D5}}\,(t) + \overline{v_{S2}}\,(t) = \\ &\overline{v_{C_{r_2}}}\,(t) - \overline{v_{C_{r_1}}}\,(t) = \\ &\overline{v_{SWPair}}\,(t) \end{aligned} \tag{65}$$

Taking into account the resonant cycles, due to the modulation strategy, there exist always either a diode or a switch conducting, within a FLCCC. Thus, leading to the following statement.

$$\overline{v_{C_{r_2}}}\,(t) - \overline{v_{C_{r_1}}}\,(t) = \begin{cases} \overline{v_{D5}}\,(t) & \text{when } S_2 \text{ conducts} \\ \overline{v_{S2}}\,(t) & \text{when } D_5 \text{ conducts} \end{cases} \tag{66}$$

Thus, exhibiting a variable voltage stress condition, upon the transition events, depending on the operating condition. In the fixed voltage-gain condition, where the current stresses are reduced, the $\overline{v_{SWPair}}\,(t)$ enlarges, introducing a larger C_{OSS} losses; whereas it reduces as Λ is reduced. In the variable voltage-gain condition, despite the fact that $\Delta v_{C_{r_n}}$ enlarges, depending on the transition event, the $\overline{v_{SWPair}}\,(t)$ is minimized and/or eliminated, exhibiting a potential benefit and increase in the overall efficiency despite of the higher current stresses. Fig. 14 demonstrates the switch pair S_2D_5 under variable voltage-gain condition, where the switch pair is exposed to ZVS as a result of the split-charge mechanism when the resonant capacitors' differential voltage is null. In contrast, the switch pair is also exposed to non-ZVS condition when the switch S_2 turns ON. However, the switch S_2's voltage stress reduces to V_{IN} as a result of the operation under the resonance where the 4L-RFLCC operates in discontinuous conduction mode, taking place within every idle state, for switches $S_1 - S_3$. Thus, reducing the C_{OSS}'s hard-switching losses.

While recent works have explored the resonant flying capacitor converter with low $\Delta v_{C_{r_n}}$, Section II demonstrate that the hard-switching losses can be attenuated, or even eliminated, by operating the converter under the right condition.

IV. DESIGN METHODOLOGY

The analysis, shown in Section II and III, indicates a level of flexibility in terms of solutions to fulfill a set of criteria, due to a equivalent effect into the large-signal based on the parameter Λ. Despite of exhibiting different degrees of freedom, the input requirements, such as the output voltage range, voltage gain, and maximum load condition, impose limitation in the characteristic impedance Z_r and switching frequency f_{SW} choices.

As shown in Section C, having a large Λ tends to decrease the normalized current stresses but inhibits the possibility of achieving variable voltage gain condition. On the contrary, having a small Λ introduces the flexibility of achieving a wider voltage gain requirement despite of the higher normalized current stresses. Although not fully covered by ZVS, having a smaller Λ also partially compensates the higher current stresses due to the inherent lower differential voltage $\overline{v_{SWPair}}\,(t)$, within each switch pair, upon every transition event.

Although increasing Λ can be perceived as a way to minimize the conduction stresses, its impact is only applicable within the same solution but ruled out when comparing different solutions, due to Z_r's relationship to the normalized current, as shown in (17). On the other hand, Λ affects directly the total passive component volume as well as $\Delta\overline{v_{C_{r_n}}}$ due to its impact on Z_r.

In order to fulfill the ZCS condition, each resonance cycle shall meet the following requirement.

$$\omega_0 \geq \frac{3}{2} \cdot 2\pi \cdot f_{SW} \tag{67}$$

By manipulating (8) and (41), the following three equations define the set of resonant components for a specific solution.

$$Z_r = \frac{1}{\pi} \cdot \frac{R_{OUT} \cdot \mu_o}{\Lambda} \tag{68}$$

Thus,

$$C_r = \frac{1}{Z_r \cdot \omega_0} \tag{69}$$

$$L_r = \frac{1}{{\omega_0}^2 \cdot C_r} \tag{70}$$

V. EXPERIMENTAL RESULTS & VALIDATION

In order to verify the theoretical assessment, and extend the utilization of the proposed converter, a 500W GaN-based prototype has been built, based on the target specifications, and calculated parameters, shown in Table 2.

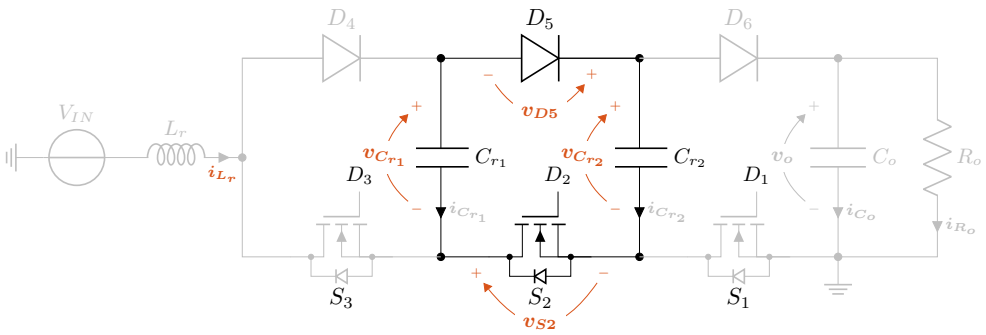

FIGURE 13. 4L-RFLCC Flying Capacitor Commutation Cell definition, emphasizing the differential mode connection, within a Switch Pair, according to two adjacent capacitors.

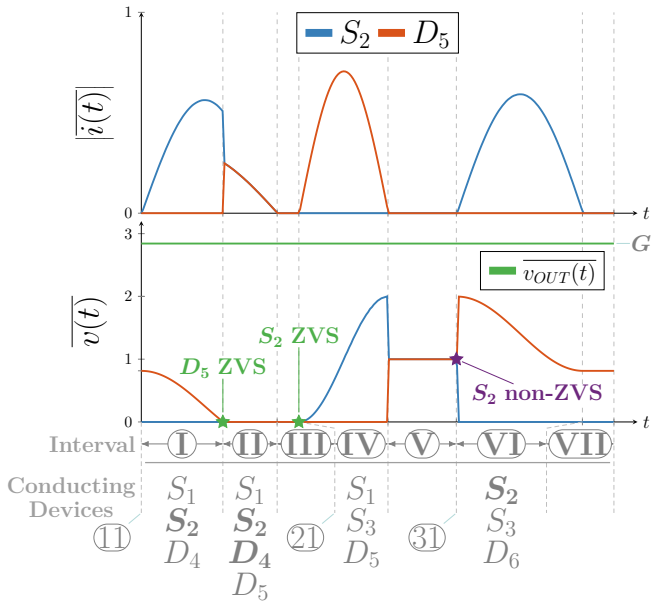

FIGURE 14. Switch Pair S_2D_5's Current and Voltage Stresses under variable voltage-gain condition featuring ZCS, ZVS and non-ZVS condition due to split-charge mechanism and under resonance operation.

TABLE 2. Target 4LRFLCC Prototype Design Specifications.

Target Prototype Design Specification	
Parameter	**Value**
Maximum DC Input Voltage	133.33 V
Maximum DC Voltage Gain	3
Maximum Output Power	530 W
Maximum Switching Frequency	500 kHz
Operating Condition $\mathbf{\Lambda}$	6
Calculated Parameters	
Resonant Capacitor $\boldsymbol{C_r}$	19.87 nF
Resonant Inductor $\boldsymbol{L_r}$	2.27 μH

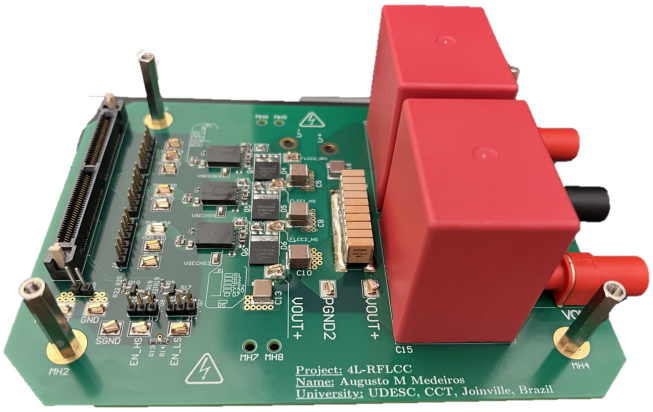

FIGURE 15. Prototype Board for 4L-RFLCC validation comprising a Texas Instruments' ControlCard, Power Stage and Buffer Capacitors, with Dimensions 153x110mm (Width x Depth).

The target operating condition $\mathbf{\Lambda}$ has been chosen in order to fulfill the maximum DC voltage gain at full Load condition. Fig. 15 shows the assembled prototype, which comprises of the three LS switches $S_1 - S_3$, Infineon (GaN Systems) GS-065-018-2-L, and three HS switches $S_4 - S_6$, Wolfspeed C6D10065Q , whereas the gate driver architecture consists of an isolated gate driver AHV85110, with Power-thru technology, from Allegro MicroSystems. The resonant tank is composed by one air-core inductor with 15 turns while the resonant capacitors are composed by two KEMET KC-LINK MLCC connected in parallel, with 12nF (CKC21C123JEGACAUTO) and 6.8nF (CKC21C682KWGACAUTO).

Fig. 16 exhibits the large-signal comparison in between the theoretical and experimental results. It leads to an acceptable correlation with the theoretical expectation. However, it does demonstrate a mismatching in both operating conditions. Despite of great effort and methods to describe the output impedance characteristic, by operating the converter with $\Lambda \leq 6$, the output impedance is inherent to the static-gain characteristic, whereas the resultant ON-resistances' losses,

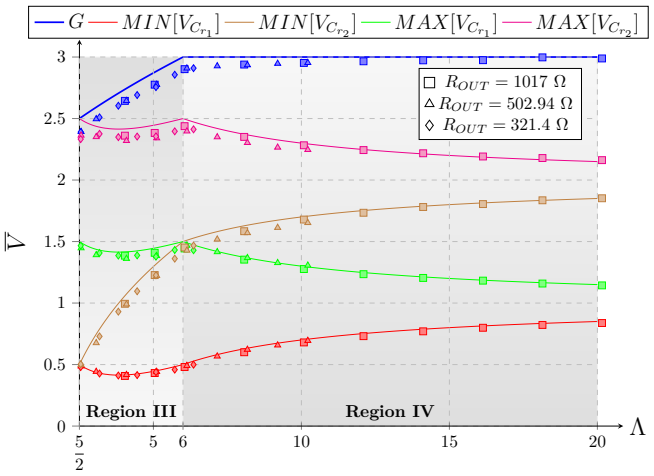

FIGURE 16. Output Static Gain & Large-Signal Characteristics Experimental Results Correlation as a function of Λ.

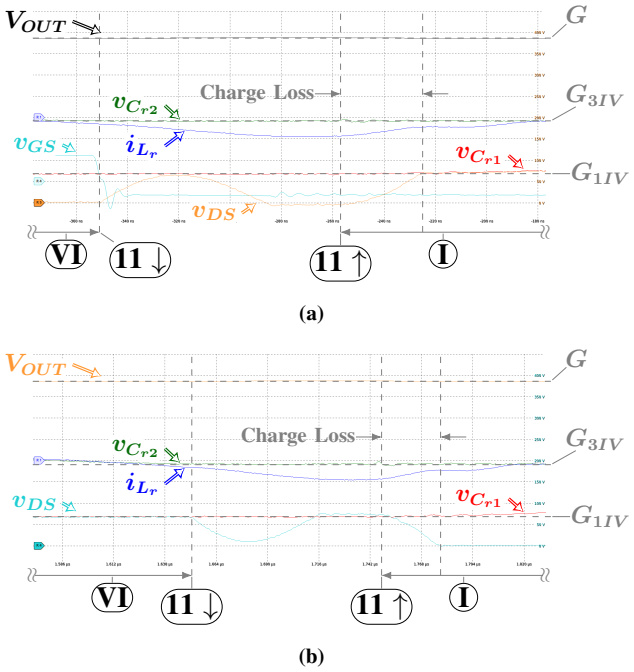

FIGURE 17. (a) Active Switch S_3's and (b) Passive Switch D_4's voltage waveform upon Transition State (11).
i_{L_r} $(5A/div)$ $v_{C_{r_1}}, v_{C_{r_2}}, v_{DS}$ **and** v_{OUT} $(50V/div)$ **and** v_{GS} $(5V/div)$ **.**
Time Scale = 20ns and Time Scale = 26ns, respectively.

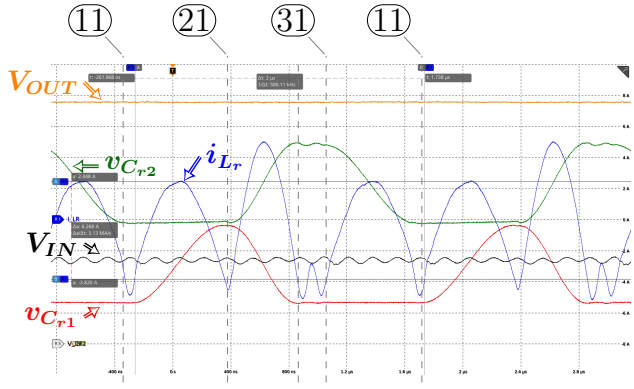

FIGURE 18. 4L-RFLCC Main State Variables' Experimental results for: $R_{OUT} = 321.4\Omega$ **and** $f_{SW} = 500kHz$ **-** i_{L_r} $(2A/div)$ $v_{C_{r_1}}, v_{C_{r_2}}, v_{IN}$ **and** v_{OUT} $(50V/div)$**. Time Scale = 400ns/div.**

also described as the Fast Switching Limit (FSL), are more predominant when operating with $\Lambda \gg 6$.

Firstly, the voltage mismatch has an ascending characteristic, which can demonstrate the effect of the ON-resistances while the charge is accumulated over each of the resonant capacitors. Additionally, Fig. 17 shows a C_{OSS} charge-loss behavior due to the non-ZVS operation, which intrinsically modifies the state-plane trajectories by initiating at a non-zero current condition upon the switch node voltage clamping. This stage can be equivalent to the split-charge mechanism observed upon the transition event (11). Thus, modifying the effective charge transferred during the topological stage thereupon.

A. Fixed Voltage Gain Condition

Fig. 18 exhibits the main state variables' experimental results ($i_{L_r}, v_{C_{r_1}}, v_{C_{r_2}}$, v_{OUT} and v_{IN} under $f_{SW} = 500kHz$ and $R_{OUT} = 321\Omega$ operating condition. It coincides closely with the target specifications, in which the state variables as well as static-gain have a good correlation with the expected results. The state variables' trajectory are synchronized with the transition states, in which the idle states are negligible, with the exception to the topological stage (IV) due to the increased resonant frequency ω_2, as expected due to the $L_r C_{r_1} C_{r_2}$ resonant tank configuration.

As a result of the DCM, the idle states are highlighted by a high-frequency oscillation, observed in the state variable i_{L_r} in Fig. 18. It results from a LC resonant tank composed by L_r and the HS and LS disabled switches' Output Capacitance C_{OSS} from the switch pair S_2 and D_5. The same is observed with more clarity in Fig. 19 where, upon the discontinuity, the v_{DS} oscillates with an initial condition, corresponding to the $v_{C_{r_2}} - v_{C_{r_1}}$, to a voltage's equilibrium point of V_{IN}.

B. Variable Voltage Gain Condition

Fig. 20 shows the main state variables' experimental results ($i_{L_r}, v_{C_{r_1}}, v_{C_{r_2}}$, v_{OUT} and v_{IN}) under $R_{OUT} = 321\Omega$ and $f_{SW} = 300kHz$ and operating condition, corresponding to $\Lambda = 3.81$, as defined by (55). In this scenario, the converter operates under a variable voltage gain condition, given an output load condition by utilizing f_{SW} as the control variable.

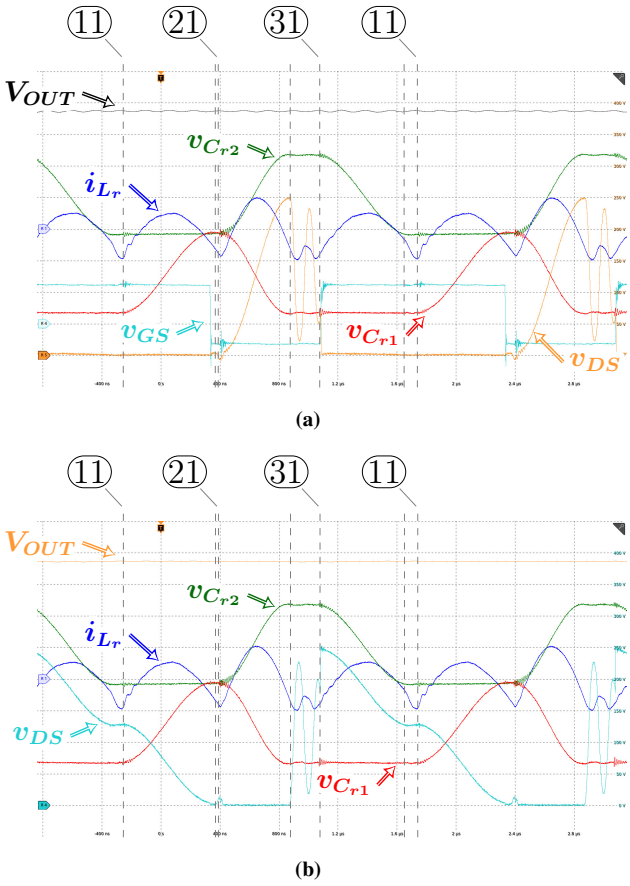

FIGURE 19. 4L-RFLCC Prototype's Switch Pair Voltage Stress Experimental Results i_{L_r} $(5A/div)$, v_{GS} $(5V/div)$,$v_{C_{r_1}}, v_{C_{r_2}}, v_{DS}$ **and** v_{OUT} $(50V/div)$ **under** $R_{OUT} = 321.4\Omega$ **and** $f_{SW} = 500kHz$ **for: ((a)) Active Switch** S_2 **((b)) Passive Switch** D_5**. Time Scale = 400ns/div.**

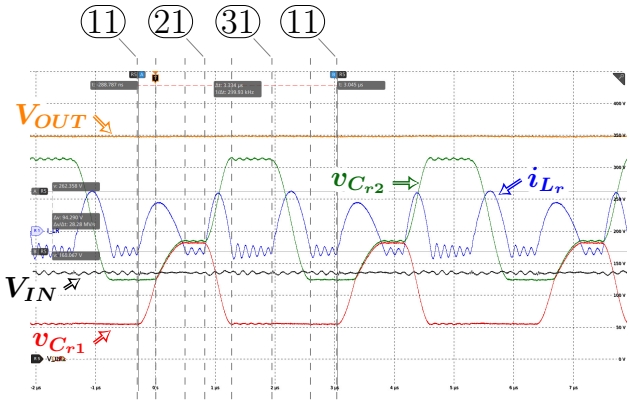

FIGURE 20. 4L-RFLCC Main State Variables' Experimental results for:$R_{OUT} = 321.4\Omega$ **and** $f_{SW} = 300kHz$ **-** i_{L_r} $(5A/div)$ $v_{C_{r_1}}, v_{C_{r_2}}, v_{IN}$ **and** v_{OUT} $(50V/div)$**. Time Scale = 1000ns/div.**

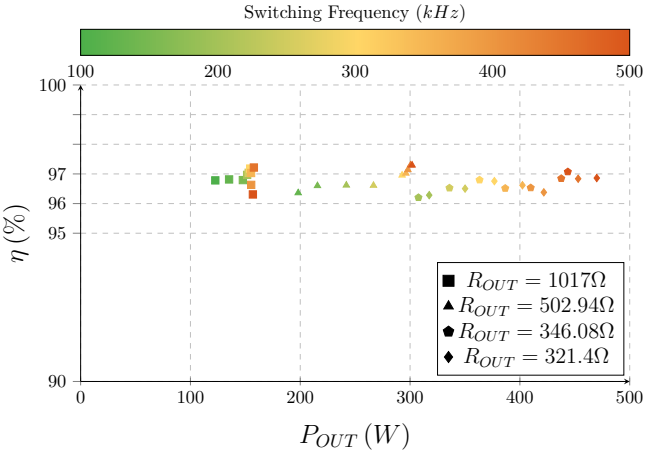

FIGURE 21. 4L-RFLCC Efficiency map featuring a flat-profile across different operating conditions while achieving high efficiency at very high switching frequencies.

The experimental results also exhibit a good correlation with the expected results, where its operating principle is highlighted by C_{r_1} and C_{r_2} voltage coupling and, thus, a split-charge mechanism within the transition state (11) state. Although $i_{C_{r_n}}$ has not been captured, this operating condition exhibits a current discontinuity, at the start of Interval (II), yielding a potential oscillation in between the switch pair S_3D_4 and S_2D_5, which, if substantial, is apparent in $v_{C_{r_n}}$.

C. Efficiency

The proposed 4L-RFLCC has demonstrated a flat efficiency profile across the operating conditions under evaluation, given different load conditions, as shown in Fig. 21 where the colormap corresponds to the switching frequency in kHz. This behavior aligns with the balance in between current stresses and switch pairs' differential voltage stress. A maximum efficiency of 97.287% has been achieved while operating the converter at 500kHz and 502.94Ω.

VI. CONCLUSION

In this work, the operation of a 4L-RFLCC under the resonance, while intentionally exhibiting low Λ conditions, is explored in order to assess its capacity to have variable voltage gain while maintaining low current stresses and soft-switching. Firstly, a succinct description of the equivalent resonant tank configuration is done which enables a comprehensive assessment of the different operating conditions while operating under low Λ conditions. Compared with the recent works, this work has shown the possibility of utilizing the 4L-RFLCC with variable voltage condition, introducing a split-charge mechanism, while maintaining soft-switching characteristic. The theoretical analysis is validated with a 530W GaN-based converter, demonstrating good correlation despite of small mismatches within the large-signal charac-

teristics, which are due to the effective ON-Resistance as well as charge-loss upon Non-ZVS operation.

VII. ACKNOWLEDGMENT

This work was partially supported by the Conselho Nacional de Desenvolvimento Científico e Tecnológico (CNPq), Brazil, under grants 402175/2022-0 and 200163/2022-1, and by the Fundação de Amparo à Pesquisa e Inovação do Estado de Santa Catarina, under grant FAPESC 2023TR000924, and also supported by Volvo Car AB, Sweden.

AUTHOR'S CONTRIBUTIONS

A. M. MEDEIROS: Conceptualization, Data Curation, Formal Analysis, Investigation, Methodology, Software, Validation, Visualization, Writing – Original Draft, Writing – Review & Editing. **Y.R. NOVAES:** Conceptualization, Formal Analysis, Investigation, Methodology, Validation, Visualization, Writing – Review & Editing.

PLAGIARISM POLICY

This article was submitted to the similarity system provided by Crossref and powered by iThenticate – Similarity Check.

REFERENCES

[1] J. Zhang, T. Q. Zheng, X. Yang, M. Wang, "Single resonant cell based multilevel soft-switching DC-DC converter for medium voltage conversion", *in 2016 IEEE Energy Conversion Congress and Exposition (ECCE)*, pp. 1–5, IEEE, Milwaukee, WI, USA, Sep. 2016, doi:10.1109/ECCE.2016.7855437, URL: http://ieeexplore.ieee.org/document/7855437/.

[2] Z. Ye, Y. Lei, R. C. N. Pilawa-Podgurski, "A resonant switched capacitor based 4-to-1 bus converter achieving 2180 W/in3 power density and 98.9% peak efficiency", *in 2018 IEEE Applied Power Electronics Conference and Exposition (APEC)*, pp. 121–126, Mar. 2018, doi:10.1109/APEC.2018.8340997, iSSN: 2470-6647.

[3] R. C. Pilawa-Podgurski, D. M. Giuliano, D. J. Perreault, "Merged two-stage power converterarchitecture with softcharging switched-capacitor energy transfer", *in 2008 IEEE Power Electronics Specialists Conference*, pp. 4008–4015, Jun. 2008, doi:10.1109/PESC.2008.4592581, iSSN: 2377-6617.

[4] R. C. N. Pilawa-Podgurski, D. J. Perreault, "Merged Two-Stage Power Converter With Soft Charging Switched-Capacitor Stage in 180 nm CMOS", *IEEE Journal of Solid-State Circuits*, vol. 47, no. 7, pp. 1557–1567, Jul. 2012, doi:10.1109/JSSC.2012.2191325.

[5] M. Vasic, D. Serrano, V. Toral, P. Alou, J. A. Oliver, J. A. Cobos, "Ultraefficient Voltage Doubler Based on a GaN Resonant Switched-Capacitor Converter", *IEEE Journal of Emerging and Selected Topics in Power Electronics*, vol. 7, no. 2, pp. 622–635, Jun. 2019, doi:10.1109/JESTPE.2019.2899180, URL: https://ieeexplore.ieee.org/document/8641359/.

[6] N. C. Brooks, S. Coday, M. E. Blackwell, R. A. Abramson, N. M. Ellis, R. C. N. Pilawa-Podgurski, "Operation of Flying Capacitor Multilevel Converters At and Above Resonance", *in 2022 IEEE 23rd Workshop on Control and Modeling for Power Electronics (COMPEL)*, pp. 1–7, IEEE, Tel Aviv, Israel, Jun. 2022, doi:10.1109/COMPEL53829.2022.9830004, URL: https://ieeexplore.ieee.org/document/9830004/.

[7] M. Shoyama, T. Naka, T. Ninomiya, "Resonant switched capacitor converter with high efficiency", *in 2004 IEEE 35th Annual Power Electronics Specialists Conference (IEEE Cat. No.04CH37551)*, pp. 3780–3786, IEEE, Aachen, Germany, 2004, doi:10.1109/PESC.2004.1355143, URL: http://ieeexplore.ieee.org/document/1355143/.

[8] W. C. Liu, T. Ge, R. C. N. Pilawa-Podgurski, "A Bi-Lateral Energy Resonant Conversion (BERC) Technique for Improved Passive Utilization in Hybrid Switched-Capacitor Converters", *IEEE Open Journal of Power Electronics*, vol. 3, pp. 772–786, 2022, doi:10.1109/OJPEL.2022.3215539.

[9] T. Ge, Z. Ye, R. C. Pilawa-Podgurski, "Geometrical State-Plane Analysis of Resonant Switched-Capacitor Converters: Demonstration on the Cascaded Multi-Resonant Converter", *IEEE Transactions on Power Electronics*, pp. 1–17, 2023, doi:10.1109/TPEL.2023.3259951.

[10] Z. Ye, S. R. Sanders, R. C. N. Pilawa-Podgurski, "Modeling and Comparison of Passive Component Volume of Hybrid Resonant Switched-Capacitor Converters", *in 2019 20th Workshop on Control and Modeling for Power Electronics (COMPEL)*, pp. 1–8, Jun. 2019, doi:10.1109/COMPEL.2019.8769707, iSSN: 1093-5142.

[11] N. M. Ellis, N. C. Brooks, M. E. Blackwell, R. A. Abramson, S. Coday, R. C. N. Pilawa-Podgurski, "A General Analysis of Resonant Switched-Capacitor Converters Using Peak Energy Storage and Switch Stress Including Ripple", *IEEE Transactions on Power Electronics*, vol. 39, no. 7, pp. 8363–8383, Jul. 2024, doi:10.1109/TPEL.2023.3285745, URL: https://ieeexplore.ieee.org/document/10159166/.

[12] R. A. Abramson, S. Coday, N. C. Brooks, M. E. Blackwell, N. M. Ellis, R. C. N. Pilawa-Podgurski, "Multi-Ratio Operation of Flying Capacitor Multilevel Converters At and Above Resonance", *in 2022 IEEE 7th Southern Power Electronics Conference (SPEC)*, pp. 1–7, IEEE, Nadi, Fiji, Dec. 2022, doi:10.1109/SPEC55080.2022.10058297, URL: https://ieeexplore.ieee.org/document/10058297/.

[13] N. C. Brooks, R. K. Iyer, R. S. Bayliss, R. C. N. Pilawa-Podgurski, "Fundamental State-Space Modeling Methodology for the Flying Capacitor Multilevel Converter", *in 2022 IEEE 23rd Workshop on Control and Modeling for Power Electronics (COMPEL)*, pp. 1–7, IEEE, Tel Aviv, Israel, Jun. 2022, doi:10.1109/COMPEL53829.2022.9830006, URL: https://ieeexplore.ieee.org/document/9830006/.

[14] T. Ge, Z. Ye, R. A. Abramson, R. C. Pilawa-Podgurski, "A 48-to-12 V Cascaded Resonant Switched-Capacitor Converter Achieving 4068 W/in ^{3} Power Density and 99.0% Peak Efficiency", *in 2021 IEEE Applied Power Electronics Conference and Exposition (APEC)*, pp. 1335–1342, IEEE, Phoenix, AZ, USA, Jun. 2021, doi:10.1109/APEC42165.2021.9487264, URL: https://ieeexplore.ieee.org/document/9487264/.

[15] F. P. Ivo Barbi, *Soft Commutation Isolated DC-DC Converters*, 1st ed., Springer Cham, 2019, doi:10.1007/978-3-319-96178-1.

BIOGRAPHIES

Augusto Manfroi Medeiros received the B.Sc. degree and M.Sc. in electrical engineering from Universidade do Estado de Santa Catarina, Joinville, Brazil, in 2016 and 2024, respectively. He has an industrial background in research and development of power electronic converters with focus on different applications. He is currently with OAK Amplifiers, Sweden. His research interests include high-frequency power conversion systems, and topologies, resonant-type converters, and magnetic components.

Yales Rômulo de Novaes (Member, IEEE) was born in Indaial, Santa Catarina, Brazil, in 1974. He received the B.S. degree in electrical engineering from the Regional University of Blumenau (FURB), Blumenau, Brazil, in 1999, and the M.Eng. and Ph.D. degrees from the Power Electronics Institute (INEP), Federal University of Santa Catarina, Florianópolis, Brazil, in 2000 and 2006, respectively. In 2001, he worked as a Research Engineer at the same institute. From 2006 to 2008, he was a Postdoctoral Fellow at the Industrial Electronics Laboratory, École Polytechnique Fédérale de Lausanne, Lausanne, Switzerland. From 2008 to 2010, he was a Scientist with the Power Electronics Systems Group, ABB Corporate Research Center, Daetwill, Switzerland. He was also a Post-Doctoral Researcher Fellow at The University of Nottingham, PEMC, UK, from 2022 to 2023. He is currently a Full Professor at UDESC - Santa Catarina State University, Joinville, Brazil, and a Coordinator of CMEAR (Research Cell on Microgrids of Alternative and Renewable Energies).